A 3D framework for geological media with multiple intersected fractures Coupled Darcy flow and Fickian diffusion

Wang, Luyu; Chen, Weizhong; Vuik, Cornelis

DOI
10.1016/j.jrmge.2024.11.043

Publication date
2025

Document Version
Final published version

Published in
Journal of Rock Mechanics and Geotechnical Engineering

Journal of Rock Mechanics and Geotechnical Engineering 17 (2025) 6293–6307

Contents lists available at ScienceDirect

Journal of Rock Mechanics and Geotechnical Engineering

journal homepage: www.jrmge.cn

Full Length Article

A 3D framework for geological media with multiple intersected fractures: Coupled Darcy flow and Fickian diffusion

Luyu Wang [a], Weizhong Chen [b, *], Cornelis Vuik [c]

[a] Department of Civil and Environmental Engineering, The Hong Kong Polytechnic University, Hung Hom, Kowloon, Hong Kong, China
[b] Institute of Rock and Soil Mechanics, Chinese Academy of Sciences, Wuhan, 430071, China
[c] Department of Applied Mathematics, Delft University of Technology, 2628 CD, Delft, The Netherlands

ARTICLE INFO

Article history:
Received 5 July 2024
Received in revised form
4 November 2024
Accepted 20 November 2024
Available online 2 January 2025

Keywords:
Fractured rock masses
3D multiple fractures
Convection-diffusion
Darcy flow
Fickian diffusion

ABSTRACT

Despite extensive research on computational geomechanics and fluid dynamics, accurately simulating convection-diffusion (CD) processes in complex fractured systems remains a significant challenge. This study develops a 3D numerical framework for modelling CD processes in fractured geological media. The framework integrates Darcy's law and Fick's law, considering flux interactions between the matrix and fractures. The meshing strategy generates high-quality grids even in scenarios involving intersecting fractures. Then, a unified numerical scheme for solving the CD system is proposed. The novelties of this work include: (1) The proposed framework enables effective simulation of 3D fractured media, including more complex fractured vuggy media; (2) The numerical method precisely discretizes the CD terms in governing equations; (3) A Non-Orthogonal Correction (NOC) method, combined with an adaptive time integration scheme, is proposed for eliminating errors induced by skewed grids; and (4) The effects of fracture patterns and heterogeneity on flow are thoroughly analysed. The proposed method is validated through benchmark tests, demonstrating the superiority of the NOC method compared to classical methods. Further analysis reveals the evolution characteristics of pressure and concentration, offering insights into the effects of fracture patterns and heterogeneity on flow and diffusion processes.

1. Introduction

Understanding fluid flow and mass transport in fractured media is paramount in a variety of geotechnical engineering and geoscience, including groundwater flow, tunnel engineering, energy exploration, and reservoir engineering (Berkowitz, 2002; Chen et al., 2021; Tan et al., 2021). Natural fractures in the real-world introduce complexities that significantly affect the behaviour of fluid flow and solute transport, making accurate modelling and simulation crucial for reliable prediction and assessment (Kolditz et al., 2012a,b; de Borst, 2017). Convection-diffusion processes are fundamental in characterising the hydraulic properties of geological media. The coupling between convection and diffusion governs the spread of contaminants and the transport of nutrients in subsurface environments (Kolditz et al., 2012a,b; Royer, 2019; Zhou et al., 2023). This process involves the combined effects of convection (fluid flow) and diffusion (molecular spreading) in transporting substances like heat or solutes within fluids. Convection carries the substance with fluid flow, while diffusion spreads it from areas of higher to lower concentration (Todd and Mays, 2004; Royer, 2019). The intricate interplay in fractured media necessitates sophisticated modelling approaches for accurate analyses. To address the issue, this study focuses on developing a comprehensive approach to simulate convection-diffusion processes in 3D fractured media.

While numerous 2D simulation methods have been employed to simulate fluid flow and transport in fractured systems, the evolving demands of practical applications necessitate a change towards 3D problems. Numerical methods for 2D fractured media have showed significant development. However, extending these methods to 3D problems introduces new challenges. In 3D models, fractures are characterised by spatial planes for flat fractures (Boon et al., 2018; Hu and Rutqvist, 2020; Wang et al., 2022a; Wong and Cui, 2023) or irregular surfaces for curved fractures (Zheng et al., 2015; Karimi-Fard and Durlofsky, 2016; Li and Zhang, 2021; Wang and Yin, 2023). Additionally, numerical treatment of multiple

* Corresponding author.
E-mail addresses: luyu.wang@polyu.edu.hk (L. Wang), wzchen@whrsm.ac.cn (W. Chen), c.vuik@tudelft.nl (C. Vuik).

https://doi.org/10.1016/j.jrmge.2024.11.043

intersecting 3D fractures remains difficult. In geological contexts, the presence of discontinues, typically discrete fractures and vugs (also known as inclusions), further complicates meshing of the computational domain. This issue has become an obstacle in 3D simulation.

In numerical simulations, fractured media can be basically modelled through two different approaches: the implicit and explicit representations of fractures. Among the numerous existing models, the equivalent continuum model (ECM) and the discrete fracture model (DFM) serve as two representative approaches. The ECM, utilizing an upscaling approach, is an efficient model to capture the hydraulic properties of fractured media by using the equivalent permeability tensor (Aguilar-López et al., 2020; Wang et al., 2022b). This attractive feature obviates the need for explicitly representing fractures. However, its accuracy depends on the proper calculation of the equivalent tensors. Notably, ECM lacks the explicit expression of fractures, resulting in an implicit description of flux connections of between fractures and matrix. An improved modelling method, DFM, has been developed, which enables consideration of flux connections between the rock matrix and fractures (Karimi-Fard et al., 2004; Martin et al., 2005; Wang et al., 2022b). The concept of DFM has also been widely applied in the mechanical analysis of rock masses (Kolditz et al., 2012a,b; Zhou et al., 2023). Remarkably, this model allows high-contrast hydraulic properties between fractures and rock matrix, a capability that is not addressed in the ECM.

Although the DFM has demonstrated success in various geoscience applications, there are still unexplored issues that deserve in-depth analysis (Kolditz et al., 2012a,b; de Borst, 2017; Chen et al., 2021). To clarify this, we categorize these issues into three main aspects: (1) modelling and meshing of 3D complex geometries; (2) flux interaction of fractures-matrix; (3) numerical stability and accuracy. The challenges outlined in the first aspect have been extensively explored in the existing literature (Hyman et al., 2014; Karimi-Fard and Durlofsky, 2016; Zidane and Firoozabadi, 2018; Fumagalli et al., 2019), and we do not intend to allocate additional space to further elaborate on it. In the second issue, fractured media differs from porous media (without fractures), primarily due to the necessity of accounting for the interaction between fractures and rock matrix (Wang et al., 2022a,c). Moreover, this challenge is intricately related to the mesh quality addressed in the first aspect. The conforming and non-conforming grids stand out as two typical solutions to address this matter. Many researchers have studied the point in detail (Karimi-Fard and Durlofsky, 2016; Zidane and Firoozabadi, 2018; Fumagalli et al., 2019). The concern mentioned in the third aspect also depends on the mesh quality and is influenced by the numerical treatment of fractures-matrix interaction. The implicit time integration requires the construction of the Jacobian matrices at each iteration, which consists of huge amount (even hundreds of thousands) of matrix elements (Jiang and Tchelepi, 2019; Wang and Yin, 2023). Moreover, skewed grids often lead to numerical instability and reduced accuracy. Although several correction approaches have been developed to migrate error from distorted grids, they have been predominantly applied within the field of computational fluid dynamics community (Jasak, 1996; Jasak and Tukovic, 2006; Demirdžić, 2015). These methods in geotechnical engineering remains limited, particularly in dealing with intricate problems like convection-diffusion in 3D fractured media. This gap highlights the necessity for further development of tailored numerical techniques that can handle the unique challenges in geotechnical simulations. Expanding the use of grid correction methods to this field could improve the accuracy and reliability of numerical models.

Considering the aforementioned challenges, this study aims to develop a robust modelling and simulation approach for convection-diffusion phenomena in 3D fractured media, with an emphasis on capturing the intricate behaviours of flow and transport. Our primary focus is on the following questions: (1) establishing an effective modelling framework for 3D complex fractured geological media; (2) developing an accurate numerical discretization method for the convection and diffusion terms in the governing equations; (3) proposing an approach to correct errors induced by skewed grids; and (4) investigating the effects of fracture patterns and material heterogeneity on convection-diffusion process.

This paper is structured as follows. In Section 2, a formulation for convection-diffusion phenomena in 3D fractured media is proposed, with consideration of flux interactions of matrix-fractures. Section 3 presents the numerical formulation, which combines an effective meshing strategy, the Non-Orthogonal Correction (NOC) method, and adaptive implicit time integration scheme. The model setup is outlined in Section 4. Section 5 provides numerical examples investigating the effects of fracture patterns and heterogeneity on convection-diffusion process.

2. Model formulation

This section presents the formulation of the convection-diffusion process in fractured media. First, a hybrid-dimensional model is introduced to describe fractured media configuration. Then, the convection-diffusion equation, incorporating Darcy's law and Fick's law, is applied to fractures and rock matrix by considering the flux interaction of matrix-fractures.

2.1. The hybrid-dimensional model of 3D fractured media

Fractures and vugs are two basic types of discontinuities commonly observed in geological formations. Depending on the characteristics of these discontinuities, two representative models can be established: fractured porous media (FPM) (Hoteit and Firoozabadi, 2018; Wang et al., 2023) and fractured vuggy porous media (FVPM) (Golfier et al., 2015; Wang et al., 2022b).

As depicted in Fig. 1a, the FPM comprises two primary constituents: the discrete fractures denoted as Ω_f, and the bulk region, often referred to as the rock matrix, denoted by Ω_m. The number of fractures is N_f, so the entire medium Ω is given by

$$\Omega = \Omega_f \cup \Omega_m \tag{1a}$$

$$\Omega_f = \cup_{i=1}^{N_f} \omega_{f,i} \tag{1b}$$

where $\omega_{f,i}$ is the domain of an individual fracture labelled by subscript i. A constraint, $\Omega_f \cap \Omega_m = \varnothing$, is required to prevent overlaps.

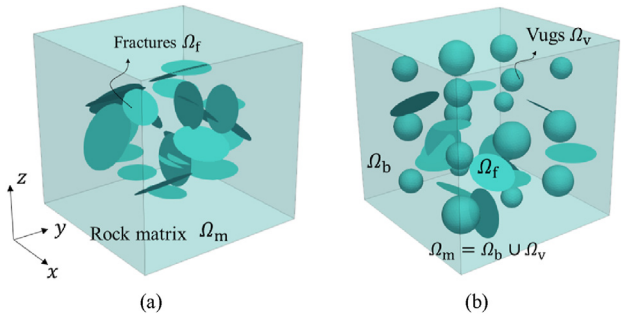

Fig. 1. Schematic of 3D computational models: (a) FPM, and (b) FVPM.

The hybrid-dimensional modelling technique is a widely adopted approach for characterising fractured media (Wang et al., 2022c, 2023). It implies that the dimension of the matrix component Ω_m is higher than that of the fractures Ω_f, expressed as

$$\Omega_m \subset \mathbb{R}^d, \Omega_f \subset \mathbb{R}^{d-1}, d = 2,3 \tag{2}$$

where $\mathbb{R}^d$ represents the d-dimensional Euclidean space.

A more complex configuration is the FVPM, where the vugs represent an additional type of discontinuities (Wang et al., 2022b), as illustrated in Fig. 1b. Description of FVPM does not pose any substantial difficulties compared to FPM. These vugs, denoted as Ω_v, can be modelled as spheres embedded inside the matrix. Eq. (2) remains applicable in FVPM with an additional relation:

$$\Omega_m = \Omega_v \cup \Omega_b \tag{3a}$$

$$\Omega_v = \cup_{i=1}^{N_v} \omega_{v,i} \tag{3b}$$

where N_v is the number of vugs, $\omega_{v,i}$ is the domain of an individual vug labelled by subscript i. The constraint, $\Omega_b = \Omega_m \backslash \Omega_v$ (or $\Omega_v \cap \Omega_b = \varnothing$), must be satisfied.

The vugs Ω_v represent sub-regions within the matrix Ω_m. The distinction between Ω_v and Ω_b lies in their properties that govern convection-diffusion process, such as permeability and diffusion coefficients. To clarify this, those properties are denoted as χ_i for a material point $\boldsymbol{x}_i, (i = f, v, m)$. The subscript indicates whether this point belongs to Ω_f, Ω_v or Ω_v, expressed by

$$\boldsymbol{x}_i(\chi_i) \in \Omega_i, (i = f, m) \text{ or } (i = f, v, b) \tag{4}$$

where $i = f, m$ and $i = f, v, b$ are applicable to FPM and FVPM, respectively.

2.2. Law of mass conservation for convection-diffusion process

In a convection-diffusion process, convection function transports substances (solutes) with the fluid flow driven by pressure gradients, while diffusion disperses these solutes by concentration gradients (Todd and Mays, 2004; Royer, 2019). The governing equations on Ω can be formulated as follows. The mass conservation for a scalar quantity $C(\boldsymbol{x}, t)$ reads (LeVeque, 1992; Wang et al., 2023):

$$\frac{\partial C(\boldsymbol{x}, t)}{\partial t} + \nabla \cdot \boldsymbol{F}(\boldsymbol{x}, t) = S(\boldsymbol{x}, t) \tag{5}$$

where $\boldsymbol{F}(\boldsymbol{x}, t)$ is the flux vector, $S(\boldsymbol{x}, t)$ is the source term, and $(\boldsymbol{x}, t)$ is a spatial-temporal point.

The phenomenon is a non-reacting flow, and the fluid is composed of two components, denoted as α and β, which respectively correspond to the solute and solvent. The fractions of mass concentration, c_α and c_β, satisfy the relation $c_\alpha + c_\beta = 1$ (Todd and Mays, 2004; Bear and Cheng, 2010).

Therefore, the law of mass conservation corresponding to each of the components can be derived. The scalar terms, $C(\boldsymbol{x}, t)$ and $S(\boldsymbol{x}, t)$, and the vector term $\boldsymbol{F}(\boldsymbol{x}, t)$ are formulated as

$$\left.\begin{array}{l} \boldsymbol{F}(\boldsymbol{x}, t) = \rho c_i \boldsymbol{u} - \rho \boldsymbol{D} \nabla c_i \\ C(\boldsymbol{x}, t) = \phi \rho c_i \\ S(\boldsymbol{x}, t) = Q c_i \end{array}\right. \quad (i = \alpha, \beta) \tag{6}$$

where ϕ is the porosity of the medium, ρ is the fluid density, Q is the flux rate. The flux term $\boldsymbol{F}$ consists of convection- and diffusion-parts, which are determined by Darcy's law and Fick's law, respectively, and are expressed as (Cussler, 2009; Bear and Cheng, 2010):

$$\left.\begin{array}{l} \boldsymbol{u} = -\dfrac{\boldsymbol{k}}{\mu}(\nabla p - \rho \boldsymbol{g}) \\ \boldsymbol{J}_i = -\rho \boldsymbol{D} \nabla c_i \end{array}\right. \tag{7}$$

where $\boldsymbol{u}$ is the Darcy's velocity, $\boldsymbol{J}_i$ is the diffusion flux vector, $\boldsymbol{g}$ is the gravity acceleration, μ is the dynamic viscosity, and p is the fluid pressure. $\boldsymbol{D}$ and $\boldsymbol{k}$ are the diffusion coefficient and the permeability tensor, respectively.

By combining Eqs. (5)–(7), one obtains the convection-diffusion equation across the computational domain:

$$\frac{\partial(\phi \rho c_i)}{\partial t} + \underbrace{\nabla \cdot (\rho c_i \boldsymbol{u})}_{\text{Convection}} + \underbrace{\nabla \cdot \boldsymbol{J}_i}_{\text{Diffusion}} = c_i \rho q \text{ on } \Omega \tag{8}$$

where Q is replaced by ρq, and q is the volumetric flux rate.

By summing Eq. (8) over components α and β, combined with relation $c_\alpha + c_\beta = 1$, the total mass transport equation is derived:

$$\frac{\partial(\phi \rho)}{\partial t} + \nabla \cdot (\rho \boldsymbol{u}) = \rho q \text{ on } \Omega \tag{9}$$

2.3. Governing equations considering flux interaction of matrix-fractures

As discussed in Section 2.1, the following framework is formulated for FPM but remains valid for FVPM by replacing Ω_m with $\Omega_v \cup \Omega_b$. Considering the conditions outlined by Eqs. (2) and (4), when applying Eqs. (8) and (9) to matrix and fractures, some modifications are necessary if the flux interaction of matrix-fracture is taken into account.

In this study, we focus on pure fluid dynamics, assuming the solid skeleton is incompressible. The total mass transport equation (Eq. (9)) and Darcy's velocity (Eq. (7)) for fluid flow in the matrix part are formulated as

$$\left.\begin{array}{l} \dfrac{\partial(\phi \rho)}{\partial t} + \nabla \cdot (\rho \boldsymbol{u}_m) = Q_m \\ \boldsymbol{u}_m = -\dfrac{\boldsymbol{k}_m}{\mu}(\nabla p_m - \rho \boldsymbol{g}) \end{array}\right. \text{ on } \Omega_m \tag{10}$$

where the flux rate can be written as $Q_m = \rho q_m$.

For the fracture component, we have:

$$\left.\begin{array}{l} \dfrac{\partial(\phi \rho)}{\partial t} + \nabla \cdot \left(\rho \boldsymbol{u}_f\right) = -\rho \left(\boldsymbol{q}_{mf} \cdot \boldsymbol{n}_f\right) \\ \boldsymbol{u}_f = -\dfrac{\boldsymbol{k}_f}{\mu}\left(\nabla p_f - \rho \boldsymbol{g}\right) \end{array}\right. \text{ on } \Omega_f \tag{11}$$

where $\boldsymbol{n}_f$ is the unit normal vector at the interface of fracture–matrix, and pointing towards the matrix, as depicted in Fig. 2. $\boldsymbol{q}_{mf}$ is the volumetric flux rate that captures the flux interaction. Note that the subscripts "m" and "f" represent the matrix and fracture, respectively.

Additionally, mass conservation is satisfied at the interface (denoted Γ_{mf}) between the matrix and the fracture:

$$\rho q_m = \rho \left(\boldsymbol{q}_{mf} \cdot \boldsymbol{n}_f\right) \text{ on } \Gamma_{mf} \tag{12}$$

This equation captures fluid channels within fractured media.

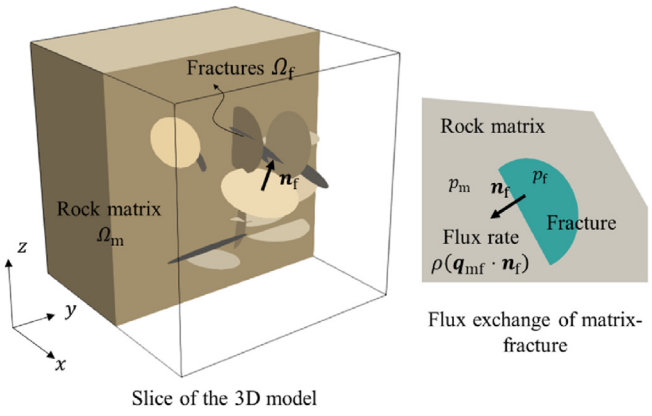

Fig. 2. Flux interaction of matrix-fracture. The flux exchange is calculated in the direction of the unit vector normal $\boldsymbol{n}_f$ to the matrix-fracture interface, pointing toward the matrix.

The flux rate can be further expressed as (Kong, 2020; Hyman et al., 2022):

$$Q_m = \rho q_m = \rho \alpha_c \frac{p_f - p_m}{2} \text{ on } \Gamma_{mf} \tag{13}$$

where the fluid channel coefficient α_c is calculated by $\alpha_c = 2k_f/(\mu a_f)$ (Martin et al., 2005; Hyman et al., 2022). a_f and k_f are aperture and isotropic permeability of the fracture, respectively.

Subsequently, taking into account the flux interaction, the convection-diffusion equation (Eq. (8)) for matrix and fracture parts is formulated for components i, expressed as

$$\frac{\partial(\phi\rho c_{m,i})}{\partial t} + \nabla\cdot(\rho c_{m,i}\,\boldsymbol{u}_m) + \nabla\cdot\boldsymbol{J}_{m,i} = c_{m,i}\,Q_m \text{ on } \Omega_m \tag{14a}$$

$$\frac{\partial\left(\phi\rho c_{f,i}\right)}{\partial t} + \nabla\cdot\left(\rho c_{f,i}\,\boldsymbol{u}_f\right) + \nabla\cdot\boldsymbol{J}_{f,i} = -c_{f,i}\,\rho\left(\boldsymbol{q}_{mf}\cdot\boldsymbol{n}_f\right) \text{ on } \Omega_f \tag{14b}$$

where the subscript i represents component α or β. Consequently, the initial boundary value problem (IBVP) is formulated as follows.

2.4. IBVP for convection-diffusion process in fractured media

In a convection-diffusion process, there are two basic types of boundary conditions. On the Dirichlet-type boundary Γ_D, one can prescribe the values of p or c_α, whereas on the Neumann-type boundary Γ_N, the gradient of these variables normal to the boundary is specified:

$$p = \overline{p} \text{ on } \Gamma_D \tag{15a}$$

$$\left.\begin{aligned} -\frac{\boldsymbol{k}}{\mu}(\nabla p)\cdot\boldsymbol{n} &= \overline{q} \\ -\boldsymbol{D}\nabla c_\alpha\cdot\boldsymbol{n} &= \overline{m} \end{aligned}\right\} \text{ on } \Gamma_N \tag{15b}$$

Since pressure p is a global variable and concentration c_α is a time-dependent variable, c_α is predefined at the initial time t_0:

$$c_\alpha = \overline{c}_\alpha \text{ at } t = t_0 \tag{16}$$

where $\overline{p}$ and $\overline{q}$ are the prescribed pressure and volumetric flux, and $\overline{c}_\alpha$ and $\overline{m}$ are the prescribed concentration and mass density.

The preceding analysis yields a well-posed formulation of the convection-diffusion system (Eqs. (10), (11) and (14)) for incompressible flow:

$$\left.\begin{aligned} &\nabla\cdot\boldsymbol{u}_m = q_m \quad \text{on } \Omega_m \\ &\nabla\cdot\boldsymbol{u}_f = -\boldsymbol{q}_{mf}\cdot\boldsymbol{n}_f \quad \text{on } \Omega_f \\ &\phi\frac{\partial c_{m,\alpha}}{\partial t} + \nabla\cdot(c_{m,\alpha}\boldsymbol{u}_m) - \nabla\cdot(\boldsymbol{D}\nabla c_{m,\alpha}) = c_{m,\alpha}\,q_m \quad \text{on } \Omega_m \\ &\phi\frac{\partial c_{f,\alpha}}{\partial t} + \nabla\cdot\left(c_{f,\alpha}\boldsymbol{u}_f\right) - \nabla\cdot\left(\boldsymbol{D}\nabla c_{f,\alpha}\right) = -c_{f,\alpha}\left(\boldsymbol{q}_{mf}\cdot\boldsymbol{n}_f\right) \quad \text{on } \Omega_f \end{aligned}\right\} \tag{17}$$

where the primary unknowns are pressure (p_m and p_f) and concentration ($c_{m,\alpha}$ and $c_{f,\alpha}$) for fluid component α, while c_β can be calculated by $1 - c_\alpha$. The convection-diffusion process is coupled with Darcy flow and Fickian diffusion through the convection term $\nabla\cdot(c_\alpha\boldsymbol{u})$ and the diffusion term $\nabla\cdot(\boldsymbol{D}\nabla c_\alpha)$, respectively.

3. Numerical method

In this section, a strategy is introduced for grid generation on a 3D complex medium. The convection and diffusion terms are discretized in a unified formulation. A correction approach is proposed to eliminate the undesirable flux induced by skewed grid cells. Then, an implicit time integration with adaptive time stepping is presented to solve the nonlinear system.

3.1. Meshing strategy and grid notations

The topological structure of a 3D fractured medium is complex, attributed to numerous intersecting fractures embedded within the matrix. Unstructured grids are generated using the Delaunay algorithm (Hyman et al., 2014; Zidane and Firoozabadi, 2018). It follows a conforming scheme, where the high-dimensional matrix cells ω_m^e are confined by the lower-dimensional fracture cells ω_f^e.

The matrix part is partitioned by the tetrahedrons, denoted as $\Omega_m = \cup_i^{N_m^e}\omega_{m,i}^e$, while the fracture part is partitioned by triangles, denoted as $\Omega_f = \cup_i^{N_f^e}\omega_{f,i}^e$. Mesh partition on the entire fractured matrix can be expressed as

$$\Omega = \left(\cup_i^{N_m^e}\omega_{m,i}^e\right)\cup\left(\cup_i^{N_f^e}\omega_{f,i}^e\right) \tag{18}$$

where N_f^e and N_m^e are numbers of fracture and matrix cells, respectively.

Particularly, dealing with the intersection of fractures introduces specific complexities. $\omega_{m,k}^e$ should align with the intersecting line formed by two crossing fractures ($\omega_{f,i}^e$ and $\omega_{f,j}^e$). Failing to achieve this might lead to unphysical overlaps of grid cells. The meshing strategy outlined in study (Wang et al., 2022a) is utilized, and additional details can be found in (Hyman et al., 2014; Karimi-Fard and Durlofsky, 2016; Zidane and Firoozabadi, 2018; Fumagalli et al., 2019).

3.2. Discretization of the convection term

The coupled system Eq. (17) is discretized using an accurate numerical scheme on the basis of the finite volume method (FVM) (Jasak, 1996; Eymard et al., 2000). To address this, temporal-spatial integrals are applied over a time interval Δt and a control volume $\omega_{*,P}$ ($* = f, m$) (in short V_P) with a centered point P:

$$\left.\begin{aligned}
&\int_{V_P}\nabla\cdot\boldsymbol{u}_{\mathrm{m}}\mathrm{d}V=\int_{V_P}q_{\mathrm{m}}\mathrm{d}V\\
&\int_{V_P}\nabla\cdot\boldsymbol{u}_{\mathrm{f}}\mathrm{d}V=\int_{V_P}-\boldsymbol{q}_{\mathrm{mf}}\cdot\boldsymbol{n}_{\mathrm{f}}\mathrm{d}V\\
&\int_{\Delta t}\int_{V_P}\left[\phi\frac{\partial c_{\mathrm{m},\alpha}}{\partial t}+\nabla\cdot\left(c_{\mathrm{m},\alpha}\boldsymbol{u}_{\mathrm{m}}\right)-\nabla\cdot\left(\boldsymbol{D}\nabla c_{\mathrm{m},\alpha}\right)\right]\mathrm{d}V\mathrm{d}t\\
&\qquad=\int_{\Delta t}\int_{V_P}c_{\mathrm{m},\alpha}\,q_{\mathrm{m}}\mathrm{d}V\mathrm{d}t\\
&\int_{\Delta t}\int_{V_P}\left[\phi\frac{\partial c_{\mathrm{f},\alpha}}{\partial t}+\nabla\cdot\left(c_{\mathrm{f},\alpha}\boldsymbol{u}_{\mathrm{f}}\right)-\nabla\cdot\left(\boldsymbol{D}\nabla c_{\mathrm{f},\alpha}\right)\right]\mathrm{d}V\mathrm{d}t\\
&\qquad=\int_{\Delta t}\int_{V_P}-c_{\mathrm{f},\alpha}\left(\boldsymbol{q}_{\mathrm{mf}}\cdot\boldsymbol{n}_{\mathrm{f}}\right)\mathrm{d}V\mathrm{d}t
\end{aligned}\right\}\tag{19}$$

Discretization of the governing equations involves both spatial and temporal aspects. The former deals with the convection and diffusion terms, while the later refers to time integration. First, the convection terms in Eq. (19) are $\nabla\cdot(c_{*,\alpha}\boldsymbol{u}_*)$ and $\nabla\cdot\boldsymbol{u}_*$. Then the general form reads

$$T_{\mathrm{cov}}=\nabla\cdot(\kappa\,\boldsymbol{u}_*)\ \ (\kappa=1\text{ or }c_{*,\alpha})\tag{20}$$

Then, it can be discretized as follows:

$$\int_{V_P}T_{\mathrm{cov}}\mathrm{d}V=\oint_{\partial V_P}\mathrm{d}\boldsymbol{A}\cdot(\kappa\,\boldsymbol{u}_*)=\sum_{S}^{N_P}\left[\boldsymbol{A}_S\cdot\left(\kappa_S\,\boldsymbol{u}_{*,S}\right)\right]\tag{21}$$

where the subscript S represents the quantities related to surface (S). The volumetric flux induced by convection across surface S can be defined using Eq. (21):

$$F_{\mathrm{cov},S}=\boldsymbol{A}_S\cdot\left(\kappa_S\,\boldsymbol{u}_{*,S}\right)\tag{22}$$

where the operator $\oint$ indicates an enclosed surface integral, N_P is the number of surfaces that enclose the control volume V_P, and $\boldsymbol{A}_S$ is the face area vector associated with surface S with the direction normal to S, as illustrated in Fig. 3a. Consequently, the discretized convection term reads

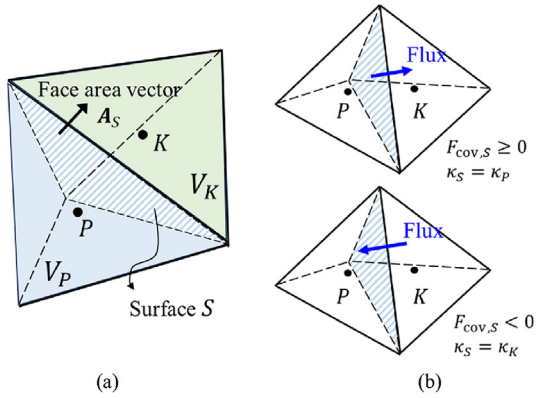

Fig. 3. Illustration of cells and parameters used in numerical discretization: (a) A pair of neighbouring cells, and (b) Upwind difference scheme.

$$\int_{V_P}\nabla\cdot(\kappa\,\boldsymbol{u}_*)\mathrm{d}V=\sum_{S}^{N_P}F_{\mathrm{cov},S}\tag{23}$$

As defined in Eq. (20), the situation is straightforward when $\kappa=1$ compared to the case when $\kappa=c_{*,\alpha}$. The value of κ across surface S can be obtained through the upwind difference scheme (Wang et al., 2022b):

$$\kappa_S=\begin{cases}\kappa_P & \text{if } F_{\mathrm{cov},S}\geq 0\\ \kappa_K & \text{if } F_{\mathrm{cov},S}<0\end{cases}\tag{24}$$

where P and K are the central points of the control volumes V_P and V_K, respectively, which share the common surface S, as depicted in Fig. 3b.

3.3. An accurate scheme for the diffusion term

The diffusion term in Eq. (19) can be generally expressed as

$$T_{\mathrm{diff}}=\nabla\cdot(\boldsymbol{D}\nabla\eta)\ \ \left(\eta=c_{\mathrm{m},\alpha},c_{\mathrm{f},\alpha}\right)\tag{25}$$

It can be discretized as follows:

$$\int_{V_P}T_{\mathrm{diff}}\mathrm{d}V=\oint_{\partial V_P}\mathrm{d}\boldsymbol{A}\cdot(\boldsymbol{D}\nabla\eta)=\sum_{S}^{N_P}\boldsymbol{A}_S\cdot\left[\boldsymbol{D}(\nabla\eta)_S\right]\tag{26}$$

where $(\nabla\eta)_S$ denotes the gradient of η across surface S. Note that the diffusion coefficient is often treated as a scalar and expressed as $\boldsymbol{D}=D\boldsymbol{I}$, where $\boldsymbol{I}$ is the identify tensor.

The volumetric flux induced by diffusion across surface S is expressed as

$$F_{\mathrm{diff},S}=\boldsymbol{A}_S\cdot\left[D(\nabla\eta)_S\right]\tag{27}$$

Consequently, the discretized diffusion term of Eq. (25) is rewritten as

$$\int_{V_P}\nabla\cdot(\boldsymbol{D}\nabla\eta)\mathrm{d}V=\sum_{S}^{N_P}F_{\mathrm{diff},S}\tag{28}$$

Notably, as shown in Fig. 4b, skewed grid cells, are more common than regular grid cells, wherein non-orthogonal grids might reduce the accuracy of the discretization method compared to the orthogonal case. The area vector $\boldsymbol{A}_S$ is decomposed into two area vectors, $\boldsymbol{A}_S=\boldsymbol{A}_S'+\boldsymbol{A}_S''$. Eq. (27) can then be reformulated as:

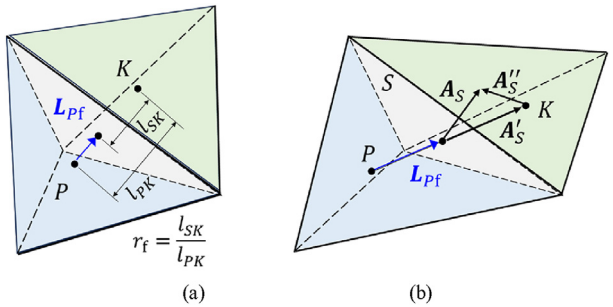

Fig. 4. Illustration of the correction approach for correcting the deviation resulting from the non-orthogonal grids: (a) Orthogonal grids and parameters, and (b) Non-orthogonal grids (skewed grids).

$$F_{\mathrm{diff},S}=\underbrace{\boldsymbol{A}_S'\cdot\left[D(\nabla\eta)_S\right]}_{\text{Orthogonal}}+\underbrace{\boldsymbol{A}_S''\cdot\left[D(\nabla\eta)_S\right]}_{\text{Non-orthogonal}} \tag{29}$$

The two terms on the right-hand side of Eq. (29) are the orthogonal and non-orthogonal parts, respectively. To improve the accuracy, we introduce an approach for correcting the non-orthogonal part (Jasak, 1996). The approach suggests that the area vectors are calculated as follows (Jasak, 1996; Demirdžić, 2015):

$$\boldsymbol{A}_S{}'=\frac{\boldsymbol{L}_{Pf}}{\boldsymbol{L}_{Pf}\cdot\boldsymbol{A}_S}|\boldsymbol{A}_S|^2 \tag{30a}$$

$$\boldsymbol{A}_S''=\boldsymbol{A}_S-\boldsymbol{A}_S{}' \tag{30b}$$

where $\boldsymbol{L}_{Pf}$ is the distance vector pointing from point P to the central point of surface S, as illustrated in Fig. 4a.

Since $\boldsymbol{A}_S{}'$ and $\boldsymbol{L}_{Pf}$ are parallel, Eq. (29) is rewritten as

$$\boldsymbol{A}_S\cdot\left[D(\nabla\eta)_S\right]=|\boldsymbol{A}_S{}'|\,D\,\frac{\eta_K-\eta_P}{\left|\boldsymbol{L}_{Pf}\right|}+\underbrace{\boldsymbol{A}_S''\cdot\left[D(\nabla\eta)_S\right]}_{\text{Correction part}} \tag{31}$$

where the correction part can not be directly derived because $\boldsymbol{A}_S''$ and $\boldsymbol{L}_{Pf}$ are not parallel. As suggested by Jasak (1996) and Jasak and Tukovic (2006) the gradient in the correction part can be obtained through interpolation:

$$(\nabla\eta)_S=r_f(\nabla\eta)_P+\left(1-r_f\right)(\nabla\eta)_K \tag{32}$$

where r_f is the interpolation factor, defined as $r_f=l_{SK}/l_{PK}$, and l_{SK} and l_{PK} are the distances of S-K and P-K, as illustrated in Fig. 4a. $(\nabla\eta)_P$ is computed by a volume gradient formula:

$$(\nabla\eta)_P=\frac{1}{V_p}\sum_S^{N_P}\boldsymbol{A}_S\,\eta_S \tag{33}$$

It is also applicable to $(\nabla\eta)_K$. The surface value η_S is determined using the upwind scheme (Wang et al., 2022b):

$$\eta_S=\begin{cases}\eta_P & \text{if } F_{\mathrm{cov},S}\geq 0\\ \eta_K & \text{if } F_{\mathrm{cov},S}<0\end{cases} \tag{34}$$

Alternatively, η_S can be calculated by the central difference, expressed by $\eta_S=r_f\,\eta_P+(1-r_f)\eta_K$.

3.4. Implicit time integration with adaptive time-stepping

The coupled system will be solved using an implicit strategy. To this end, the time-dependent term in Eq. (19) is discretized as

$$\int_{\Delta t}\int_{V_P}\phi\frac{\partial\eta}{\partial t}\mathrm{d}V\mathrm{d}t=\phi\,\frac{\eta^{n+1}-\eta^n}{\Delta t}\Delta V_P\Delta t\ \left(\eta=c_{\mathrm{m},\alpha},c_{\mathrm{f},\alpha}\right) \tag{35}$$

where n and $n+1$ represent the time steps of the previous and updated time levels, respectively.

For the convection and diffusion terms corresponding to Eqs. (23) and (28), the time integration is expressed as $\sum_S^{N_P}F_{\mathrm{cov},S}\Delta t$ and $\sum_S^{N_P}F_{\mathrm{diff},S}\Delta t$. Consequently, the discretization of the system of governing equations (Eq. (19)) can take various forms for the matrix and fracture parts. For each of the matrix cells, we have

$$\left.\begin{aligned}&\sum_S^{N_P}\left(\boldsymbol{A}_S\cdot\boldsymbol{u}_{\mathrm{m},S}^{n+1}\right)=\Delta V_P\frac{k_f}{\mu}\,\frac{\left(p_f^{n+1}-p_m^{n+1}\right)}{a_f}\\ &\phi\Delta V_P\frac{c_{\mathrm{m},\alpha}^{n+1}-c_{\mathrm{m},\alpha}^{n}}{\Delta t}+\sum_S^{N_P}\boldsymbol{A}_S\cdot\left[c_{\mathrm{m},\alpha}\,\boldsymbol{u}_{\mathrm{m},S}\right]^{n+1}\\ &\quad-\sum_S^{N_P}\boldsymbol{A}_S\cdot\left[D(\nabla c_{\mathrm{m},\alpha})_S\right]^{n+1}=c_{\mathrm{m},\alpha}^{n+1}\,\Delta V_P\,\frac{k_f}{\mu}\,\frac{\left(p_f^{n+1}-p_m^{n+1}\right)}{a_f}\end{aligned}\right\} \tag{36}$$

For each of the fracture cells:

$$\left.\begin{aligned}&\sum_S^{N_P}\left(\boldsymbol{A}_S\cdot\boldsymbol{u}_{\mathrm{f},S}^{n+1}\right)=L_{\mathrm{f},P}^2\frac{k_f}{\mu}\,\left(p_m^{n+1}-p_f^{n+1}\right)\\ &\phi\,a_f\,L_{\mathrm{f},P}\frac{c_{\mathrm{f},\alpha}^{n+1}-c_{\mathrm{f},\alpha}^{n}}{\Delta t}+\sum_S^{N_P}\boldsymbol{A}_S\cdot\left[c_{\mathrm{f},\alpha}\,\boldsymbol{u}_{\mathrm{f},S}\right]^{n+1}\\ &\quad-\sum_S^{N_P}\boldsymbol{A}_S\cdot\left[D\left(\nabla c_{\mathrm{f},\alpha}\right)_S\right]^{n+1}=c_{\mathrm{f},\alpha}^{n+1}\,L_{\mathrm{f},P}^2\,\frac{k_f}{\mu}\,\left(p_m^{n+1}-p_f^{n+1}\right)\end{aligned}\right\} \tag{37}$$

where $L_{\mathrm{f},P}$ is the characteristic length of the fracture cell V_P. The meanings of other notations have been introduced in the preceding sections. The velocities $\boldsymbol{u}_{\mathrm{m},S}$ and $\boldsymbol{u}_{\mathrm{f},S}$ in the matrix and fractures are calculated from Darcy's law (Eqs. (10) and (11)).

The Newton-Raphson method (Nithiarasu et al., 2016; Jiang and Tchelepi, 2019; Wang et al., 2022b) is used to iteratively solve the nonlinear equations (Eqs. (36) and (37)). The residual vector of primary unknowns (pressure p and concentration c_α) is defined for the matrix and fracture cells, $\boldsymbol{R}=[\boldsymbol{R}_{\mathrm{p,m}}\ \ \boldsymbol{R}_{\mathrm{p,f}}\ \ \boldsymbol{R}_{\mathrm{c,m}}\ \ \boldsymbol{R}_{\mathrm{c,f}}]^{\mathrm{T}}$. As an example, a component labelled with i in $\boldsymbol{R}_{\mathrm{c,m}}$, denoted as $[R_{\mathrm{c,m}}]_i$, reads

$$\begin{aligned}\left[R_{\mathrm{c,m}}\right]_i=&\,c_{\mathrm{m},\alpha}^{n+1}\,\Delta V_P\,\frac{k_f}{\mu}\,\frac{\left(p_f^{n+1}-p_m^{n+1}\right)}{a_f}-\phi\Delta V_P\frac{c_{\mathrm{m},\alpha}^{n+1}-c_{\mathrm{m},\alpha}^{n}}{\Delta t}\\ &-\sum_S^{N_P}\boldsymbol{A}_S\cdot\left[c_{\mathrm{m},\alpha}\,\boldsymbol{u}_{\mathrm{m},S}\right]^{n+1}+\sum_S^{N_P}\boldsymbol{A}_S\cdot\left[D(\nabla c_{\mathrm{m},\alpha})_S\right]^{n+1}\end{aligned} \tag{38}$$

During each iteration step ν, the Jacobian is formed through the derivative of residual vector with respect to the unknown vector (Jiang and Tchelepi, 2019; Wang et al., 2022b, 2023) denoted as $\boldsymbol{J}=\partial\boldsymbol{R}/\partial\boldsymbol{x}$, where $\boldsymbol{x}$ is the unknown vector, $\boldsymbol{x}=\left[\boldsymbol{p}_{\mathrm{m}}\ \ \boldsymbol{p}_{\mathrm{f}}\ \ \boldsymbol{c}_{\mathrm{m},\alpha}\ \ \boldsymbol{c}_{\mathrm{f},\alpha}\right]^{\mathrm{T}}$.

The incremental vector $\delta\boldsymbol{x}^{\nu+1}$ of unknowns at the updated iteration step $(\nu+1)$ is calculated from the algebraic system derived from the Newton-Raphson method, $\boldsymbol{J}^{\nu}\delta\boldsymbol{x}^{\nu+1}=-\boldsymbol{R}^{\nu}$, which can be written in the matrix form:

$$\underbrace{\begin{bmatrix}\boldsymbol{J}_{\mathrm{p,m}}^{\mathrm{mm}} & \boldsymbol{J}_{\mathrm{p,m}}^{\mathrm{mf}} & \boldsymbol{J}_{\mathrm{p,m}}^{\mathrm{mm}} & \boldsymbol{J}_{\mathrm{p,m}}^{\mathrm{mf}}\\ \boldsymbol{J}_{\mathrm{p,f}}^{\mathrm{fm}} & \boldsymbol{J}_{\mathrm{p,f}}^{\mathrm{ff}} & \boldsymbol{J}_{\mathrm{p,f}}^{\mathrm{fm}} & \boldsymbol{J}_{\mathrm{p,f}}^{\mathrm{ff}}\\ \boldsymbol{J}_{\mathrm{c,m}}^{\mathrm{mm}} & \boldsymbol{J}_{\mathrm{c,m}}^{\mathrm{mf}} & \boldsymbol{J}_{\mathrm{c,m}}^{\mathrm{mm}} & \boldsymbol{J}_{\mathrm{c,m}}^{\mathrm{mf}}\\ \boldsymbol{J}_{\mathrm{c,f}}^{\mathrm{fm}} & \boldsymbol{J}_{\mathrm{c,f}}^{\mathrm{ff}} & \boldsymbol{J}_{\mathrm{c,f}}^{\mathrm{fm}} & \boldsymbol{J}_{\mathrm{c,f}}^{\mathrm{ff}}\end{bmatrix}^{\nu}}_{\boldsymbol{J}^{\nu}}\underbrace{\begin{bmatrix}\delta\boldsymbol{p}_m\\ \delta\boldsymbol{p}_f\\ \delta\boldsymbol{c}_{\mathrm{m},\alpha}\\ \delta\boldsymbol{c}_{\mathrm{f},\alpha}\end{bmatrix}^{\nu+1}}_{\delta\boldsymbol{x}^{\nu+1}}=-\underbrace{\begin{bmatrix}\boldsymbol{R}_{\mathrm{p,m}}\\ \boldsymbol{R}_{\mathrm{p,f}}\\ \boldsymbol{R}_{\mathrm{c,m}}\\ \boldsymbol{R}_{\mathrm{c,f}}\end{bmatrix}^{\nu}}_{\boldsymbol{R}^{\nu}} \tag{39}$$

where the sub-Jacobi matrix $\boldsymbol{J}_{\mathrm{p,m}}^{\mathrm{mf}}$ characterises the flux interaction between fracture cells (f) and matrix cells (m), contributed by pressure (p) of the matrix cells (m). Similar explanations apply to other sub-Jacobi matrices.

Therefore, the updated unknown vector $\boldsymbol{x}^{\nu+1}$ can be obtained as the sum of $\boldsymbol{x}^{\nu+1} = \boldsymbol{x}^{\nu} + \delta\boldsymbol{x}^{\nu+1}$. The iteration Eq. (39) will be terminated upon reaching the convergence criterion:

$$\left\|\boldsymbol{R}^{n+1}\right\|_2 < \epsilon \tag{40}$$

where the tolerance ϵ is user defined and typically lies within the magnitude of $\sim 10^{-6}$. Eq. (39) represents a large algebraic system that requires iterative solvers for solution, such as BICGSTAB, GMRES, and PCG, combined with stabilized techniques (Vuik et al., 1999; Vuik, 2023). In our program, we utilize *Eigen* (Guennebaud and Jacob, 2010) to solve this system.

Commonly, Δt is a constant value defined at the initial time. Nevertheless, this approach can occasionally lead to convergence challenges and a decrease in computational efficiency (Shepherd et al., 2019; Wang and Yin, 2023). To address this concern, an adaptive iteration approach is formulated, which allows for the dynamic adjustment of Δt. Then, Δt is determined based on the following condition:

$$\Delta t = \begin{cases} r_1 \times \Delta t' & \text{if } \left\|\boldsymbol{R}^{n+1}\right\|_2 < r_c \times \epsilon \\ r_2 \times \Delta t' & \text{if } \left\|\boldsymbol{R}^{n+1}\right\|_2 > \epsilon \\ \Delta t' & \text{Otherwise} \end{cases} \tag{41}$$

where the parameters r_c, r_1 and r_2 are assigned values within the range of $0 < r_c < 1$, $0 < r_2 < 1$ and $r_1 > 1$, and $\Delta t'$ is the time increment at the previous step. A flowchart illustrating the implicit time integration with adaptive time-stepping (I-ATS) is presented in Fig. 5, where the procedure for adaptive time control is determined by Eq. (41).

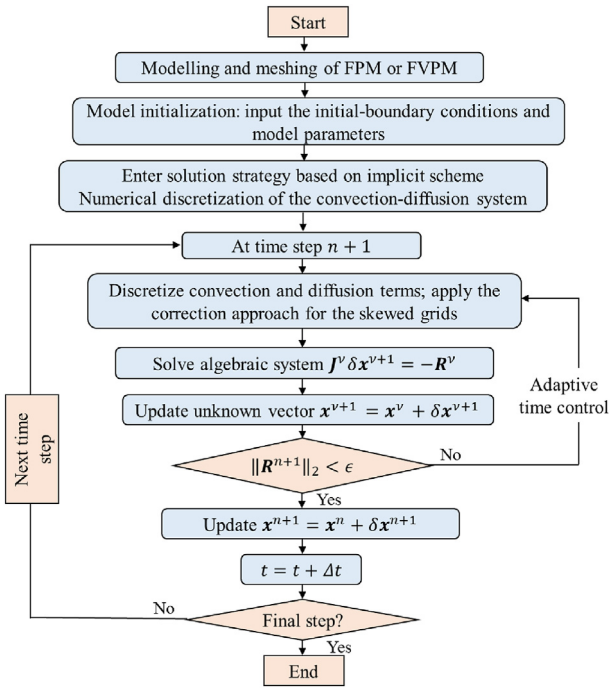

Fig. 5. Flowchart of the solution strategy.

4. Model setup and material parameters

This section provides the methodology for generating 3D fractures, accompanied by visualisation examples of the model and grids. Then, the model parameters used in simulations are given.

4.1. Generation and visualisation of 3D fractures

To construct the FPM and FVPM presented in Section 2, the geometrical parameters of each fracture should be defined. The parameters characterising a 3D fracture are: coordinates of the central point of the fracture $(x_i^{\mathrm{f}}, y_i^{\mathrm{f}}, z_i^{\mathrm{f}})$, the radius (R_i^{f}), and two angles related to fracture orientation (θ_i and θ_i') (Berkowitz, 2002; Chen et al., 2021; Wang et al., 2022a). These values are generated through a random number generator:

$$\mathrm{Rand}\left(x_i^{\mathrm{f}}, y_i^{\mathrm{f}}, z_i^{\mathrm{f}}, R_i^{\mathrm{f}}, \theta_i, \theta_i'\right) \left(i = 1 \sim N_{\mathrm{f}}\right) \tag{42}$$

It can also follow various statistical laws, such as power law, normal or logarithmic normal distributions (de Dreuzy et al., 2012; Hyman et al., 2019). In this study, we utilize the 3D fracture modelling and meshing approach developed in existing literature (Hyman et al., 2014; Karimi-Fard and Durlofsky, 2016; Wang et al., 2022a). Herein, the key aspects of this approach are summarized as follows:

(1) The meshing strategy employs a conforming generation method for unstructured grids based on the Delaunay algorithm.
(2) Delaunay tetrahedrons and triangles are used to partition the rock matrix and fractures, respectively, with matrix cells (higher-dimensional objects) assigned alongside fracture cells (lower-dimensional objects).
(3) At fracture intersection positions, cells are aligned along the intersected lines of fractures, as depicted in the inset of Fig. 6b. More details on the treatment of intersecting fractures and the interaction between vugs and fractures can be found in our previous study (Wang et al., 2022a; Karimi-Fard and Durlofsky, 2016).

As an illustration, Fig. 6 provides some visualisation examples of grids and models, demonstrating that the proposed approach can effectively generate high-quality meshes with different grid resolutions, denoted as h. The total numbers of grids

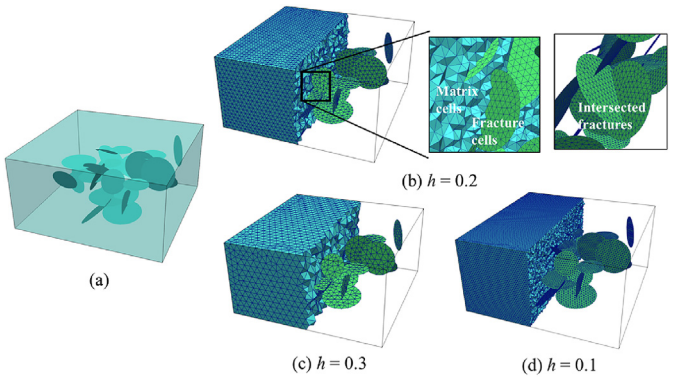

Fig. 6. Grids and model visualisation of a fractured porous medium containing multiple fractures: (a) Model configuration, (b), (c) and (d) display the meshes with different grid resolutions h.

corresponding to $h = 0.1$, 0.2, and 0.3 are approximately 26, 9.6, and 3.2×10^4, respectively.

4.2. Model parameters

The physical properties of the fractured media are summarized in Table 1. Note that these parameters used in our simulations are configured as follows, unless otherwise specified. Without loss of generality, the molecular diffusion coefficient in Fick's law (Eq. (7)) is assumed to be isotropic, given by $\boldsymbol{D} = D\mathbf{I}$. We set $D = 2.6\times 10^{-5}$ $m^2 s^{-1}$ as suggested in reference (Cussler, 2009). In this context, the solute and solvent correspond to water and air, respectively. Similarly, we consider the permeabilities $\boldsymbol{k}_m$ and $\boldsymbol{k}_f$ in Darcy's law (Eqs. (10) and (11)) to be isotropic as well.

Numerous models have been proposed to determine k_f, including some grounded in statistical theory, such as the correlated power law (Hyman et al., 2016). In the present simulation, we assume that the isotropic permeability of fracture k_f depends on the fracture aperture a_f, following the classical cubic law (Dippenaar and Van Rooy, 2016; Wang et al., 2024):

$$k_f = \frac{a_f^2}{12} \tag{43}$$

where the aperture a_f can be assigned either randomly distributed values or constant for each fracture, as studied by Bisdom et al. (2016) and Huang et al. (2019).

5. Numerical examples: Results and discussion

In this section, we begin by validating the proposed method through a benchmark study with a comparison of different methods. Then, the effect of fracture patterns on convection-diffusion processes is explored. The analysis extends to examining the role of heterogeneity within both the fractured medium and the fractured vuggy medium.

Table 1
Physical properties of the fractured media.

Properties	Values	Units
Porosity ϕ	0.2	
Fluid density ρ	1000	kg/m^3
Dynamic viscosity μ	8.9×10^{-4}	Pa s
Diffusion coefficient D	2.6×10^{-5}	m^2/s
Rock permeability k_m	$1 \times 10^{-18} - 1 \times 10^{-13}$	m^2
Fracture aperture a_f	0.05–0.5	mm
Aperture-dependent fracture permeability k_f	$2 \times 10^{-12} - 2 \times 10^{-7}$	m^2

Remarks: (1) Sources of parameters: Cussler (2009); Kong (2020); Mavko et al. (2020); Wang and Zhang (2024). (2) k_f is determined by Eq. (43).

5.1. Comparison with different methods

Before applying the proposed method to investigate more complex processes, we validate it through a benchmark study. This benchmark test is widely employed for the verification of numerical methods (Zielke et al., 1991; Berre et al., 2021). The modelling approach and numerical discretization method follow the formulation given in the preceding sections.

The benchmark model consists of a single-inclined fracture within a square shape, with dimension of 5 m × 5 m, and oriented at an angle 45° to the x-y plane. The size of the cubic computational domain is 10 m × 10 m × 10 m. The fracture is located at the center of the domain, as shown in the inset in Fig. 7. The boundary condition is specified with prescribed pressures, with the inlet and outlet set to 4 MPa and 6 MPa, respectively. Permeabilities of the matrix and fracture parts are $k_m = 10^{-15}$ m^2 and $k_f = 10^{-10}$ m^2, respectively. Obviously, k_f is significantly larger than k_m, making it a preferential channel for fluid flow. The pressure distribution is obtained until the flow reaches a steady state. In Fig. 7, the results calculated by our proposed method are compared with two existing methods: the embedded discrete fracture model (EDFM) (Ţene et al., 2017) and the method developed by Wang and Yin (2023). The simulation results demonstrate a good agreement among these methods.

To further analyse the convergence performance of the method, the variations of error and residual are required to be evaluated during the iteration process. The relative error is defined as

$$\varepsilon_h = \sum_{i=1}^{N_{node}} \frac{\|\tilde{x}_i - x_i^h\|_2}{\|\tilde{x}_i\|_2} \tag{44}$$

where $\tilde{x}_i$ is the reference solution of node i, x_i^h is the results obtained by the proposed method with different grid resolutions h. The relative error ε_h can be defined for both pressure and concentration, denoted as ε_h^p and ε_h^c. Fig. 8 shows the convergence of ε_h^p with increasing grid resolution across various permeability ratios k_m/k_f in the range of $10^{-5} \sim 10^2$ m^2. The performance of the implicit adaptive time-steeping (I-ATS) developed in Section 3.4 is evaluated and illustrated in Fig. 9. The results demonstrate that the

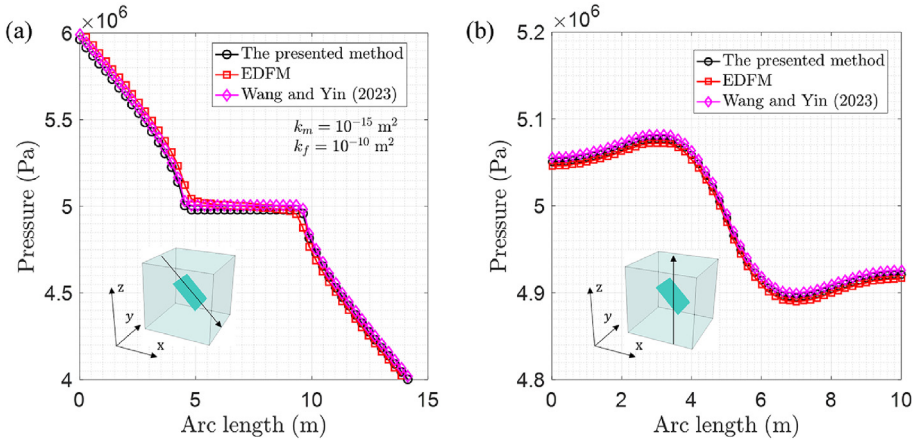

Fig. 7. Verification by comparing with solutions obtained by existing methods: Pressure distribution along (a) the diagonal and (b) the vertical direction of the model.

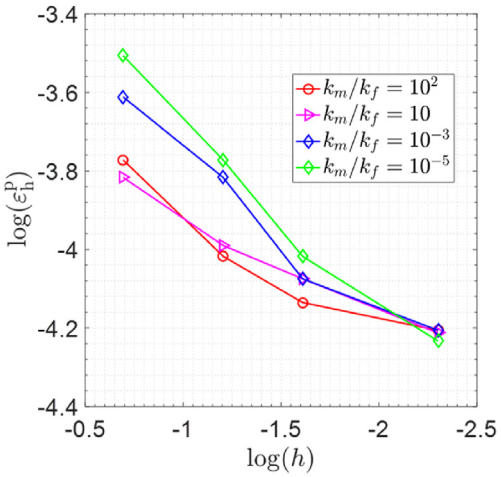

Fig. 8. Grid convergence of the proposed method applied to different material properties. k_m and k_f represent the permeabilities of rock matrix and fractures (unit: m^2), respectively. The scale of y-axis denotes $\log_{10}(\cdot)$.

I-ATS improves the speed of convergence compared to the case without ATS. In addition, with the adaptive strategy, the time increment at each iteration step is updated, rapidly decreasing to a small value. In contrast, without ATS, the time increment remains constant, resulting in slower convergence compared to the ATS method.

5.2. Effect of the NOC method on accuracy

To further examine the performance of the proposed method, an analytical model (Etori, 1992; Bodin, 2015) of convention-diffusion is used to explore the evolution of concentration c_α. The computational model is the same as the above benchmark model. To demonstrate the efficiency of the proposed NOC method, two different grid systems are established for simulating the same tests. The majority of cells in the skewed grid system (Fig. 10a) consist of distorted cells with poor properties, which may induce significant errors compared the regular grid system (Fig. 10b).

To align the model settings with the conditions required by the analytical solution, some assumptions are adopted as follows. First, the domain should be a homogeneous medium, achieved by setting $k_m = k_f$. Second, at the inlet boundary, a line source is assigned with $\bar{c}_\alpha = 1$ along the y-axis, following the analytical model, which is a 2D model with a point source (Etori, 1992; Bodin, 2015). Then,

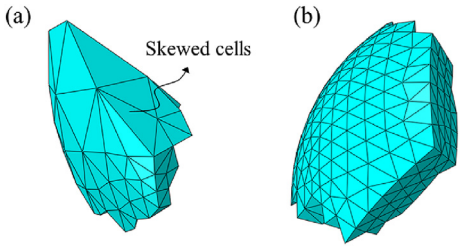

Fig. 10. Illustrations of (a) the skewed grids with poor properties (requiring correction by the NOC) and (b) the regular grids with desirable properties.

we compare the numerical results (obtained from a 2D slice cut along the y-axis) with the analytical solution, as displayed in Fig. 11a. Two representative points are chosen to illustrate the evolution of concentration over time. Points P_A and P_B are located at the center and on the boundary of the domain, with coordinates of (5,5,5) and (0,5,5), respectively.

The effect of the NOC method, developed in Section 3.3, on numerical accuracy is illustrated in Fig. 11. The results are obtained using the proposed method, with the option to either apply or omit the correction term based on the NOC method, denoted as "NOC" and "no NOC" on these curves. For comparison, the x-axis represents the normalized time throughout the convection-diffusion process. It shows a gradual decrease in the rate of concentration increase as time progresses. In this simulation, the deviation between NOC and no-NOC is not pronounced, given the high-quality meshes. However, a significant disparity will be more pronounced in conditions of lower mesh quality.

The convergence curves of the NOC method are displayed in Fig. 12. The relative error ε_h^c in concentration calculation decreases with the increasing grid resolution. As shown in Fig. 12a, the NOC method exhibits faster convergence compared to the case without NOC. These results demonstrate the superiority of NOC in handling skewed grids. In Fig. 12b, the number of iterations required to achieve a small value of residual $\log_{10}\|\boldsymbol{R}\|_2$ is smaller for the homogeneous material case ($k_m/k_f = 1$) compared to the heterogeneous case ($k_m/k_f = 10^2$). This indicates that the permeabilities of fractures (k_f) and rock matrix (k_m) significantly affect the convergence performance. One potential factor that might affect the performance of the NOC method is its computational efficiency. Unlike the method without NOC, the NOC method requires additional effort to calculate the correction term in numerical discretization. This limitation can be mitigated by ATS. Fig. 13 demonstrates that both the NOC and ATS methods are capable of

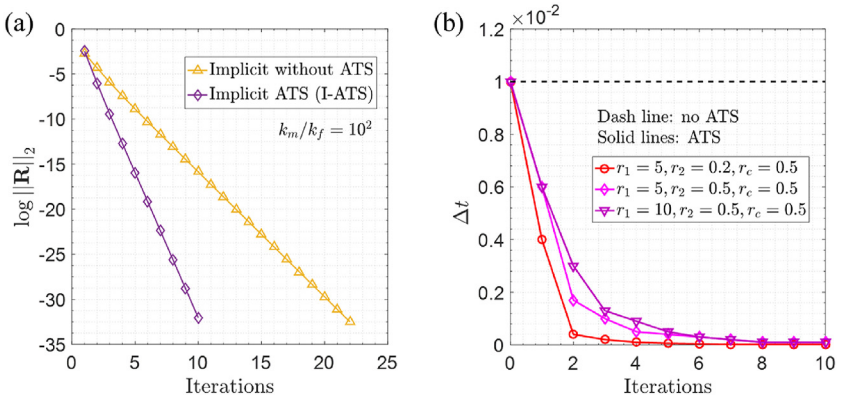

Fig. 9. Error convergence of the proposed method using implicit time integration with ATS and without ATS: (a) Variation of the L^2-norm of residual (the scale of y-axis denotes $\log_{10}(\cdot)$), and (b) Variation of time increment during iteration, determined by Eq. (41).

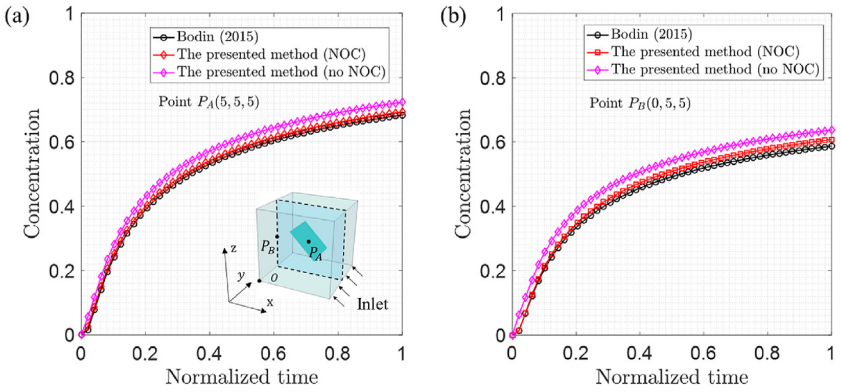

Fig. 11. Comparison between the results obtained from the existing solution (Bodin, 2015) and the proposed method with or without the NOC method.

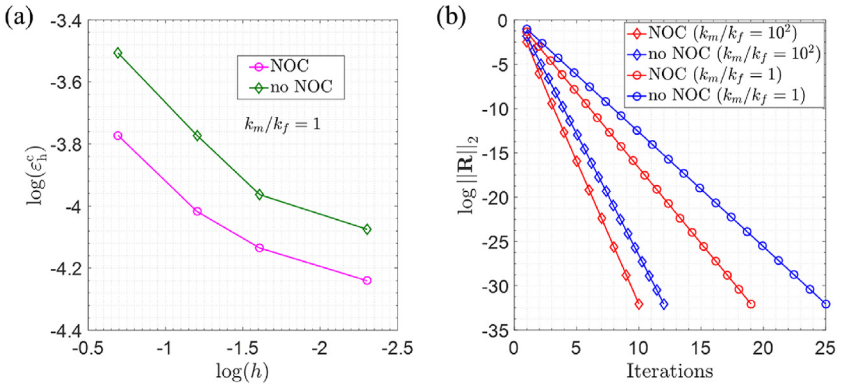

Fig. 12. Error convergence of the proposed method: (a) Variation of the error induced by concentration calculation, and (b) Variation of the L^2-norm of residual with or without NOC.

improving computational efficiency, as reflected by reductions in the total number of iterations. A reason is that the NOC method reduces errors in simulations, while the ATS dynamically adjusts the time increment to accelerate convergence.

5.3. Convection-diffusion process in 3D fractured media

Following the validations in Sections 5.1 and 5.2, this section presents the simulation results for convection-diffusion in complex 3D fractured media, considering patterns with 40 fractures, 100 fractures, and fractures-vugs. We assume that the vugs are filled with geological materials, and fluid flow follows Darcy's law. In more complex situations, such as vugs filled with fluid, Brinkman equation should be employed.

The computational domain is a cuboid with dimensions of 100 m $\times$ 100 m $\times$ 50 m. Numerous discrete fractures and vugs are randomly distributed within the domain. As depicted in Fig. 14, the pressure boundaries at the inlet and outlet are specified as 2 MPa and 5 MPa, respectively. The flow direction is aligned with the y-axis. Permeabilities k_m and k_f are set to 10^{-15} m^2 and 10^{-10} m^2, respectively. Other properties are listed in Table 1.

Given the model settings described above, the distributions of pressure and concentration in the fractured media (comprising only fractures) are illustrated in Figs. 14 and 15. The corresponding illustration for fractured vuggy media (comprising fractures-vugs) is provided in Fig. 16. The radius of the discrete fractures is 8 $\sim$ 15 m. In the situation of a fractured vuggy medium, we assign the permeabilities to the matrix, fractures and vugs as $k_\mathrm{m} = 10^{-15}$ m^2 and $k_\mathrm{f} = k_\mathrm{v} = 10^{-10}$ m^2. Therefore, both fractures and vugs act as preferential channels for fluid compared to the rock matrix.

Fig. 14 provides a slice view of the computational domain, illustrating the connectivity between the matrix cells and fractures. Evidently, the pressure distribution aligns with the direction of the pressure gradient, following the y-axis. This observation is consistent with intuitive perception. Besides, the evolution of concentration is illustrated in Fig. 15. In the scenario of 100 days, it becomes evident that the fracture network possesses a property of highly conductive channel for flow. The concentration migrating to the left-hand side of the fracture network occurs at a faster rate than in the matrix part. It reveals the fact that the presence of

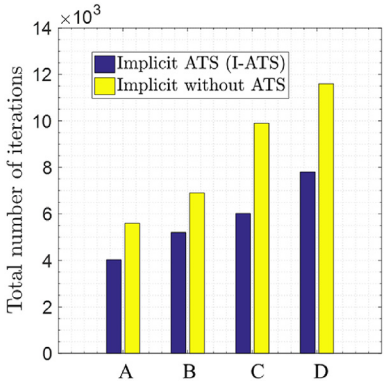

Fig. 13. Variation of the total number of iterations in simulations. A: NOC ($k_\mathrm{m}/k_\mathrm{f} = 1$); B: no NOC ($k_\mathrm{m}/k_\mathrm{f} = 1$); C: NOC ($k_\mathrm{m}/k_\mathrm{f} = 10^2$); D: no NOC ($k_\mathrm{m}/k_\mathrm{f} = 10^2$).

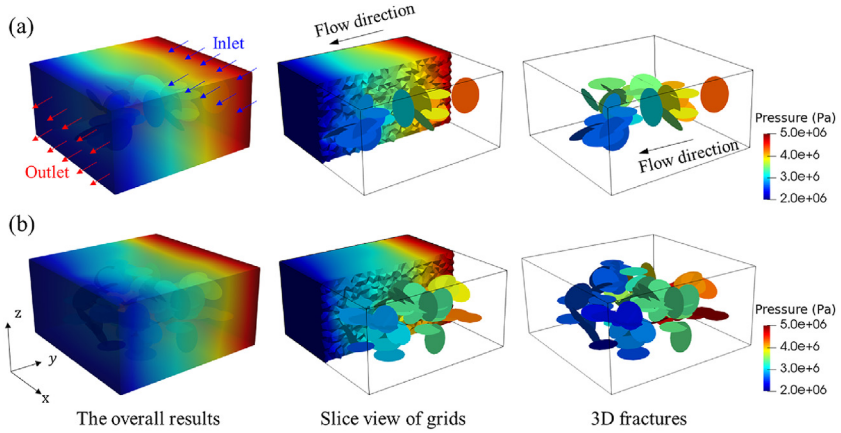

Fig. 14. Pressure distribution of fractured media with different fracture numbers: (a) 40 fractures, and (b) 100 fractures.

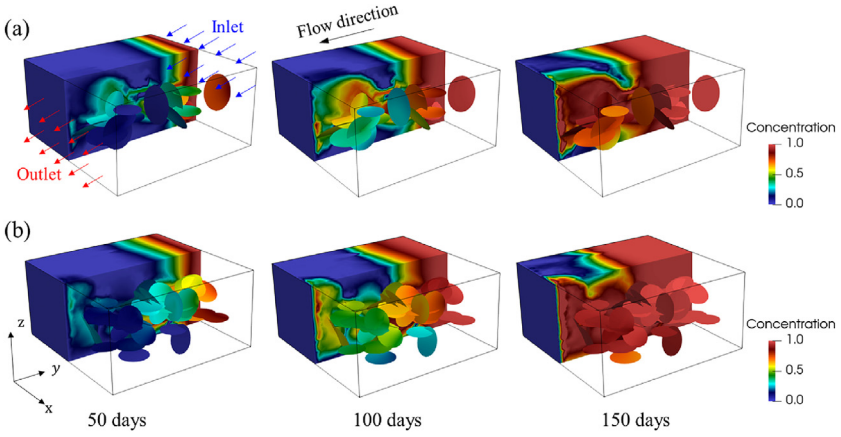

Fig. 15. Concentration evolution of fractured media with different fracture numbers: (a) 40 fractures, and (b) 100 fractures.

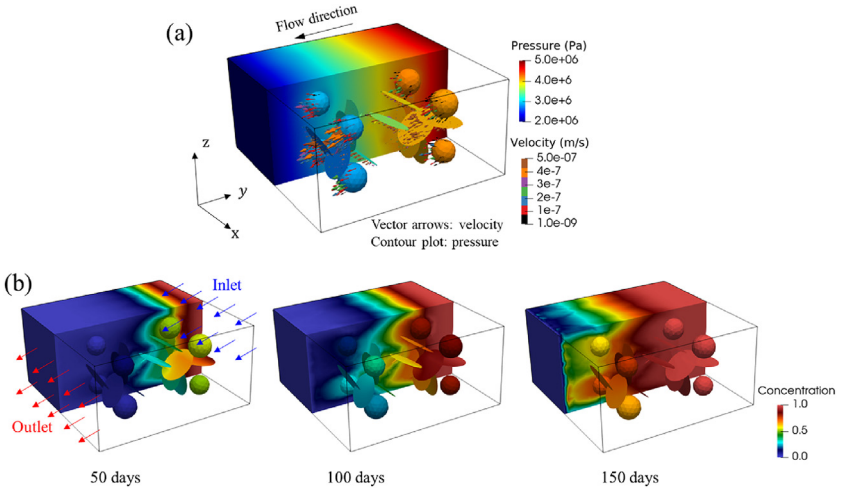

Fig. 16. Simulation results of a fractured vuggy porous medium: (a) Distributions of pressure and velocity vector arrows, and (b) Concentration evolution. Two colour bars in (a) are used for representing different quantities.

fracture network accelerates the propagation of concentration. Furthermore, through a comparison of Fig. 15a and b, it is evident that an increase in the number of fractures amplifies this effect. A large number of fractures may increase the possibility of constructing the connected-fractures, which demonstrate superior conductivity compared to the non-connected fractures.

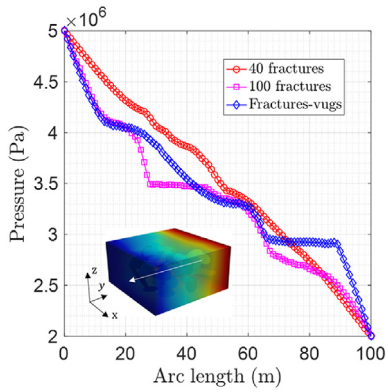

Fig. 17. Pressure distribution in the fractured media with different patterns (fractured or fractured-vuggy).

To further explore the characteristics of pressure distribution, Fig. 17 illustrates the variations in pressure distribution within a fractured medium exhibiting different patterns. The monitoring line layouts extend along the flow direction aligned with the y-axis. It illustrates that the presence of fractures alters the pressure distribution at specific local positions where they intersect, leading to distortion in the pressure curves. Those distortions are related to the geometry of fractures and vugs. For instance, the curves of pressure and concentration for 40 fractures appear relatively smoother compared to the other two cases. The concentration evolution along the diagonal of the model is presented in Fig. 18. The simulation results reveal that the concentration will ultimately approach 1. As illustrated in Fig. 18c, the concentration in approximately half of the region along the arc length (about $0 \sim 75$ m) reaches 1. This observation implies the domain is gradually saturated over time.

5.4. The role of permeability heterogeneity

In this study, model heterogeneity is characterised by generating a random distribution of permeabilities for both the rock matrix and fractures. We apply an approach for generating random permeabilities similar to that developed in (Wang et al., 2022c). To achieve this, the quantity χ_i in Eq. (4) is represented in terms of k_m and k_f. We then use the method described by Eq. (42) to generate fracture parameters, wherein the generator Rand($\cdot$) follows the normal distribution without loss of generality. Note that the aperture a_f can be adjusted to different values to reflect the heterogeneity in permeability. The results are illustrated in Fig. 19, with a more detailed depiction provided in Fig. 20. It demonstrates that the distribution aligns with the bell-shaped curve of the probability density function.

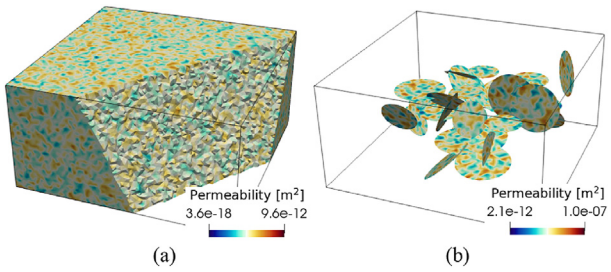

Fig. 19. Permeability distribution in a heterogeneous medium (unit: m^2): (a) Rock matrix part, and (b) Fracture part.

Convection-diffusion simulation is conducted for both heterogeneous and homogeneous cases in fractured media. The simulation results are displayed in Figs. 21 and 22. The impact of heterogeneity on pressure distribution is given in Fig. 21. The figure reveals that the existence of heterogeneous permeability results in a slight fluctuation in the pressure curve. Nonetheless, the trends in pressure variation in both heterogeneous and homogeneous scenarios are remarkably similar. Furthermore, the effect of heterogeneity on the flow rate is evident, as shown in Fig. 22. Note that the flow rate, denoted as q_r, is defined as the product of velocity and the sectional area of the outlet boundary. The flow rate ratio, denoted as $\overline{q}_\mathrm{r}$, is a normalized quantity expressed as $\overline{q}_\mathrm{r} = q_\mathrm{r}/q_\mathrm{r,m}$, where $q_\mathrm{r,m}$ is the maximum flow rate at the outlet. The simulation results show that the heterogeneity in permeability marginally increases the flow rate, while the overall characteristics remain similar to those in the homogeneous situation. The extent of the flow rate improvement depends on the value of permeability as well as its distribution characteristics.

6. Conclusions and implications

In this work, we developed a three-dimensional numerical framework for modelling convection-diffusion phenomena in fractured geological media containing multiple fractures. The main conclusions and implications are summarized as follows:

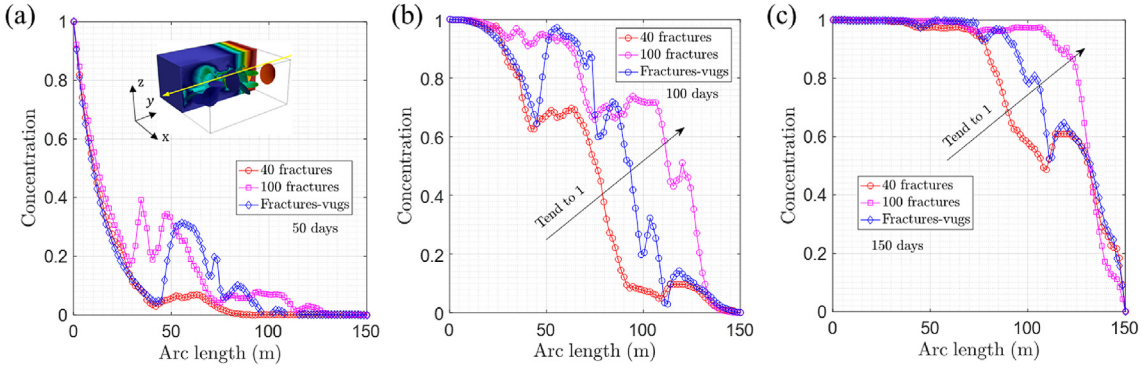

Fig. 18. Concentration evolution in the fractured media with different patterns (fractured or fractured-vuggy): (a) 50 days, (b) 100 days, and (c) 150 days.

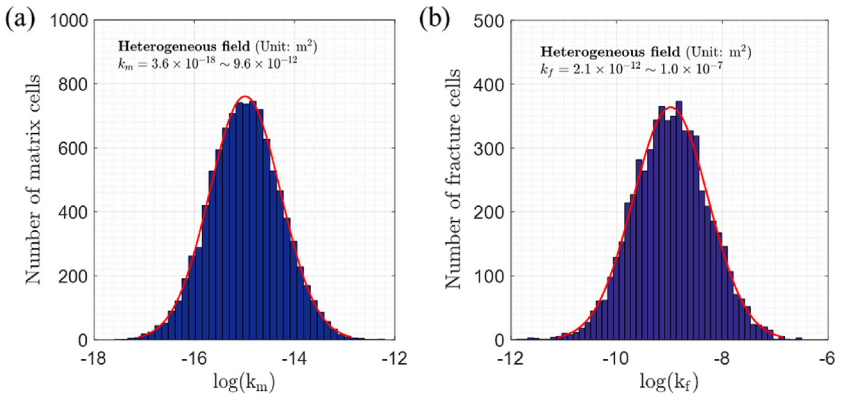

Fig. 20. Heterogeneous field generated by random permeabilities k_m and k_f for (a) the matrix part and (b) the fracture part, respectively. Note that the scale of x-axis represents $\log_{10}(\cdot)$.

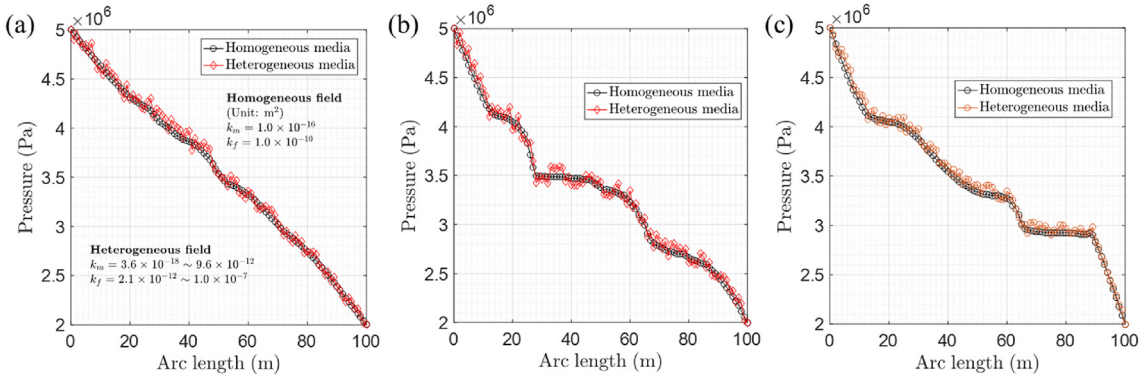

Fig. 21. Comparison between homogeneous and heterogeneous media, corresponding to Fig. 17: (a) 40 fractures, (b) 100 fractures, and (c) Fractures-vugs.

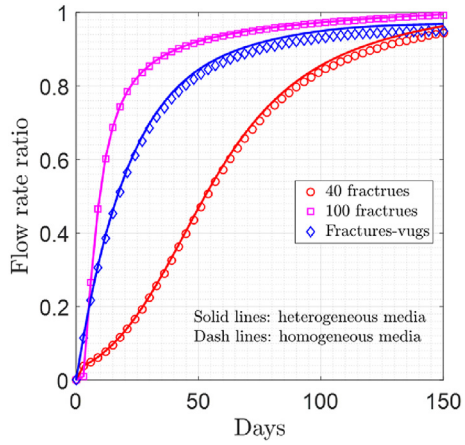

Fig. 22. The effect of permeability heterogeneity on flow rate during convection-diffusion process.

(1) The proposed method efficiently simulates both fractured porous media and complex fractured vuggy porous media. The meshing strategy generates high-quality grids even in scenarios involving complex intersecting fractures.
(2) The convection-diffusion equation is used to capture coupled processes in fractured media by incorporating flux interactions between fractures and the rock matrix. The formulation integrates Fickian diffusion and Darcy's law to establish a coupled nonlinear system.
(3) An accurate numerical discretization method is proposed for handling the convection and diffusion terms in a unified way. The NOC method is proposed to eliminate undesirable fluxes resulting from the skewed (non-orthogonal) grids. An adaptive implicit time integration scheme is used to efficiently solve the convection-diffusion system. Numerical tests demonstrate the superiority of the NOC method compared to classical methods.
(4) The proposed method was verified through benchmark tests, comparing the simulation results with those obtained from existing methods. The analysis includes a thorough examination of pressure distribution and concentration evolution in fractured media. Further analyses reveal the effects of fracture patterns and material heterogeneity on convection-diffusion process.

Some limitations of this study highlight areas for future research. On the one hand, a fully coupled numerical formulation is needed to simulate hydro-mechanical coupling in rock fractures, integrating displacement and fluid pressure within a single system. On the other hand, integrating contact constitutive laws into the presented formulation is essential to accurately describe closure, slip, stick, and shear failure of fracture surfaces, as well as for achieving stress-dependent apertures in hydro-mechanical coupling.

CRediT authorship contribution statement

Luyu Wang: Writing – original draft, Software, Methodology,

Formal analysis, Conceptualization. **Weizhong Chen:** Writing – review & editing, Supervision, Project administration, Funding acquisition. **Cornelis Vuik:** Writing – review & editing, Supervision, Methodology.

Declaration of competing interest

The authors declare that they have no known competing financial interests or personal relationships that could have appeared to influence the work reported in this paper.

Acknowledgments

This research was financially supported by the National Natural Science Foundation of China (Grant Nos. 51991392 and 42293355).

References

Aguilar-López, J.P., Bogaard, T., Gerke, H.H., 2020. Dual-Permeability model improvements for representation of preferential flow in fractured clays. Water Resour. Res. 56 (8), e2020WR027304.
Bear, J., Cheng, A.H.D., 2010. Modeling Groundwater Flow and Contaminant Transport. Springer International Publishing, Switzerland.
Berkowitz, B., 2002. Characterizing flow and transport in fractured geological media: a review. Adv. Water Resour. 25, 861–884.
Berre, I., Boon, W.M., Flemisch, B., Fumagalli, A., Gläser, D., Keilegavlen, E., Scotti, A., Stefansson, I., Tatomir, A., Brenner, K., Burbulla, S., 2021. Verification benchmarks for single-phase flow in three-dimensional fractured porous media. Adv. Water Resour. 147, 103759.
Bisdom, K., Bertotti, G., Nick, H.M., 2016. The impact of different aperture distribution models and critical stress criteria on equivalent permeability in fractured rocks. J. Geophys. Res. Solid Earth 121 (5), 4045–4063.
Bodin, J., 2015. From analytical solutions of solute transport equations to multidimensional time-domain random walk (TDRW) algorithms. Water Resour. Res. 51, 1860–1871.
Boon, W.M., Nordbotten, J.M., Yotov, I., 2018. Robust discretization of flow in fractured porous media. SIAM J. Numer. Anal. 56 (4), 2203–2233.
Chen, W., Wang, L., Tan, X., Yang, D., Yuan, J., Yang, J., 2021. State-of-the-art and development tendency of the underground engineering stability of fractured rock mass. Chinese J. Rock Mech. Eng. 10, 945–1961 (in Chinese).
Cussler, E.L., 2009. Diffusion: Mass Transfer in Fluid Systems, third ed. Cambridge University Press, Cambridge, UK.
de Borst, R., 2017. Fluid flow in fractured and fracturing porous media: a unified view. Mech. Res. Commun. 80, 47–57.
de Dreuzy, J.R., Méheust, Y., Pichot, G., 2012. Influence of fracture scale heterogeneity on the flow properties of three-dimensional discrete fracture networks (DFN). J. Geophys. Res. Solid Earth 117 (B11), 1–21.
Demirdžić, I., 2015. On the discretization of the diffusion term in finite-volume continuum mechanics. Numer. Heat Tran. B 68 (1), 1–10.
Dippenaar, M.A., Van Rooy, J.L., 2016. On the cubic law and variably saturated flow through discrete open rough-walled discontinuities. Int. J. Rock Mech. Min. Sci. 89, 200–211.
Etori, K., 1992. Solution of a diffusion equation of smoke molecules due to constant point source in gravitational field. Lett. Math. Phys. 26, 271–275.
Eymard, R., Gallouët, T., Herbin, R., 2000. Finite volume methods. In: Ciarlet, P.G. (Ed.), Handbook of Numerical Analysis, vol. 7. Elsevier, the Netherlands, pp. 713–1018.
Fumagalli, A., Keilegavlen, E., Scialò, S., 2019. Conforming, non-conforming and non-matching discretization couplings in discrete fracture network simulations. J. Comput. Phys. 376, 694–712.
Golfier, F., Lasseux, D., Quintard, M., 2015. Investigation of the effective permeability of vuggy or fractured porous media from a Darcy-Brinkman approach. Comput. Geosci. 19, 63–78.
Guennebaud, G., Jacob, B., 2010. Eigen. http://eigen.tuxfamily.org. (Accessed 1 June 2024).
Hoteit, H., Firoozabadi, A., 2018. Modeling of multicomponent diffusions and natural convection in unfractured and fractured media by discontinuous Galerkin and mixed methods. Int. J. Numer. Methods Eng. 114 (5), 535–556.
Hu, M., Rutqvist, J., 2020. Numerical manifold method modeling of coupled processes in fractured geological media at multiple scales. J. Rock Mech. Geotech. Eng. 12, 667-618.
Huang, N., Jiang, Y., Liu, R., Li, B., Sugimoto, S., 2019. A novel three-dimensional discrete fracture network model for investigating the role of aperture heterogeneity on fluid flow through fractured rock masses. Int. J. Rock Mech. Min. Sci. 116, 25–37.
Hyman, J.D., Gable, C.W., Painter, S.L., Makedonska, N., 2014. Conforming delaunay triangulation of stochastically generated three dimensional discrete fracture networks: a feature rejection algorithm for meshing strategy. SIAM J. Sci. Comput. 36, A1871–A1894.
Hyman, J.D., Aldrich, G., Viswanathan, H., Makedonska, N., Karra, S., 2016. Fracture size and transmissivity correlations: implications for transport simulations in sparse three-dimensional discrete fracture networks following a truncated power law distribution of fracture size. Water Resour. Res. 52 (8), 6472–6489.
Hyman, J.D., Dentz, M., Hagberg, A., Kang, P.K., 2019. Linking structural and transport properties in three-dimensional fracture networks. J. Geophys. Res. Solid Earth 124 (2), 1185–1204.
Hyman, J.D., Sweeney, M.R., Gable, C.W., Svyatsky, D., Lipnikov, K., David Moulton, J., 2022. Flow and transport in three-dimensional discrete fracture matrix models using mimetic finite difference on a conforming multi-dimensional mesh. J. Comput. Phys. 466 (1), 111396.
Jasak, H., Tukovic, Z., 2006. Automatic mesh motion for the unstructured finite volume method. Trans. FAMENA 30 (2), 1–20.
Jasak, H., 1996. Error Analysis and Estimation for the Finite Volume Method with Applications to Fluid Flows. University of London, England, UK. Ph.D. thesis.
Jiang, J., Tchelepi, H.A., 2019. Nonlinear acceleration of sequential fully implicit (SFI) method for coupled flow and transport in porous media. Comput. Methods Appl. Mech. Eng. 352, 246–275.
Karimi-Fard, M., Durlofsky, L.J., 2016. A general gridding, discretization, and coarsening methodology for modeling flow in porous formations with discrete geological features. Adv. Water Resour. 96, 354–372.
Karimi-Fard, M., Durlofsky, L.J., Aziz, K., 2004. An efficient discrete-fracture model applicable for general-purpose reservoir simulators. SPE J. 9, 227–236.
Kolditz, O., Bauer, S., Bilke, L., Böttcher, N., Delfs, J.O., Fischer, T., Görke, U.J., Kalbacher, T., Kosakowski, G., McDermott, C.I., et al., 2012a. OpenGeoSys: an open-source initiative for numerical simulation of thermo-hydro-mechanical/chemical (THM/C) processes in porous media. Environ. Earth Sci. 67 (2), 589–599.
Kolditz, O., Görke, U.J., Shao, H., Wang, W., 2012b. Thermo-hydro-mechanical-chemical Processes in Fractured Porous Media. Springer Science & Business Media, Berlin, Germany.
Kong, X., 2020. Advanced Mechanics of Fluids in Porous Media, third ed. University of Science and Technology of China Press, Hefei, China.
LeVeque, R.J., 1992. Numerical Methods for Conservation Laws. Birkhäuser Verlag, Basel, Switzerland.
Li, S., Zhang, D., 2021. Development of 3D curved fracture swarms in shale rock driven by rapid fluid pressure buildup: insights from numerical modeling. Geophys. Res. Lett. 47 (8), e2021GL092638.
Martin, V., Jaffré, J., Roberts, J.E., 2005. Modeling fractures and barriers as interfaces for flow in porous media. SIAM J. Sci. Comput. 26 (5), 1667–1691.
Mavko, G., Mukerji, T., Dvorkin, J., 2020. The Rock Physics Handbook, third ed. Cambridge University Press, MA, US.
Nithiarasu, P., Lewis, R.W., Seetharamu, K.N., 2016. Fundamentals of the Finite Element Method for Heat and Mass Transfer, second ed. John Wiley & Sons, New York, US.
Royer, P., 2019. Advection–diffusion in porous media with low scale separation: modelling via higher-order asymptotic homogenisation. Transport Porous Media 128, 511–551.
Shepherd, D., Miles, J., Heil, M., Mihajlović, M., 2019. An adaptive step implicit midpoint rule for the time integration of Newton's linearisations of non-linear problems with applications in micromagnetics. J. Sci. Comput. 80, 1058–1082.
Tan, X., Chen, W., Wang, L., Yang, J., Tan, X., 2021. Settlement behaviors investigation for underwater tunnel considering the impacts of fractured medium and water pressure. Mar. Georesour. Geotechnol. 39 (6), 639–648.
Țene, M., Bosma, S.B., Al Kobaisi, M.S., Hajibeygi, H., 2017. Projection-based embedded discrete fracture model (pEDFM). Adv. Water Resour. 105, 205–216.
Todd, D.K., Mays, L.W., 2004. Groundwater Hydrology, third ed. John Wiley & Sons, New York, US.
Vuik, C., Segal, A., Meijerink, J.A., 1999. An efficient preconditioned CG method for the solution of a class of layered problems with extreme contrasts in the coefficients. J. Comput. Phys. 152 (1), 385–403.
Vuik, C., 2023. Iterative Solution Methods. Delft Institute of Applied Mathematics, Delft, the Netherlands.
Wang, L., Wang, Y., Vuik, C., Hajibeygi, H., 2022a. Accurate modeling and simulation of seepage in 3D heterogeneous fractured porous media with complex structures. Comput. Geotech. 156, 105273.
Wang, L., Golfier, F., Tinet, A.J., Chen, W., Vuik, C., 2022b. An efficient adaptive implicit scheme with equivalent continuum approach for two-phase flow in fractured vuggy porous media. Adv. Water Resour. 163, 104186.
Wang, L., Chen, W., Vuik, C., 2022c. Hybrid-dimensional modelling for fluid flow in heterogeneous porous media using dual fracture-pore model with flux interaction of fracture-cavity network. J. Nat. Gas Sci. Eng. 100, 104450.
Wang, L., Chen, W., Zhang, Y., Vuik, C., 2023. Investigating Effects of Heterogeneity and Fracture Distribution on Two-phase Flow in Fractured Reservoir with Adaptive Time Strategy, vol. 9. Trans Porous Media, pp. 1–29.
Wang, L., Yin, Z.Y., 2023. Fluid flow and mass transport in fractured media with curved fractures and varying apertures: a 3D modeling approach. Int. J. Numer. Methods Eng. 124 (19), 4311–4338.
Wang, L., Zhang, Y., 2024. Interpreting correlations in stress-dependent permeability, porosity, and compressibility of rocks: a viewpoint from finite strain theory. Int. J. Numer. Anal. Methods GeoMech. 48 (8), 2000–2019.
Wang, L., Chen, W., Sui, Q., 2024. Study of hydro-mechanical behaviours of rough rock fracture with shear dilatancy and asperities using shear-flow model. J. Rock Mech. Geotech. Eng. 16 (10), 4004–4016.
Wong, L.N.Y., Cui, X., 2023. Simulation of 3D fracture propagation under I-II-III

mixed-mode loading. Rock Mech. Bull. (Arch. Am. Art) 2 (4), 100082.
Zheng, Y., Xia, L., Yu, Q., 2015. A method for identifying three-dimensional rock blocks formed by curved fractures. Comput. Geotech. 65, 1–11.
Zhou, C.B., Chen, Y.F., Hu, R., Yang, Z., 2023. Groundwater flow through fractured rocks and seepage control in geotechnical engineering: theories and practices. J. Rock Mech. Geotech. Eng. 15 (1), 1–36.
Zidane, A., Firoozabadi, A., 2018. Reservoir simulation of fractured media in compressible single-phase flow in 2D, 2.5D and 3D unstructured gridding. Adv. Water Resour. 121, 68–96.
Zielke, W., Helmig, R., Krohn, K.P., Shao, H., Wollrath, J., 1991. Discrete modelling of transport processes in fractured porous rock. In: 7th International Congress on Rock Mechanics (ISRM) Congress. Aachen, Germany. ISRM-7CONGRESS-1991-013.

Dr. Luyu Wang obtained his BSc degree in mining engineering from Shandong University of Science and Technology, and his PhD degree in geotechnical engineering at Wuhan Institute of Rock and Soil Mechanics. He is now a postdoctoral fellow at The Hong Kong Polytechnic University (PolyU), Hong Kong, China. Before joining PolyU, he was a visiting PhD student at Delft University of Technology, The Netherlands, and pursued his postdoctoral career at CNRS-GeoRessources Lab., France. His research interests include damage and fracture of geomaterials, flow and transport in fractured porous media, and multi-physics coupling in geosciences.